

Indian Head Division
Naval Surface Warfare Center
Indian Head, MD 20640-5035

IHTR 2168
16 April 1999

MECHANICAL THRESHOLD STRESS CONSTITUTIVE STRENGTH MODEL DESCRIPTION OF HY-100 STEEL

*D.M. Goto
R.K. Garrett, Jr.
Indian Head Division
Naval Surface Warfare Center*

*J. Bingert
Shuh-Rong Chen
George T. Gray, III
Los Alamos National Laboratory
Los Alamos, NM*

Approved for public release; distribution is unlimited.



DTIC QUALITY INSPECTED 4

20000202 042



FOREWORD

This work was sponsored by the Office of Naval Research (Code 333, Dr. Judah Goldwasser) and the Internal Laboratory Independent Research program at Indian Head Division, NSWC. The authors also acknowledge the technical assistance of Drs. Paul Maudlin and George Kaschner and Messrs. Mike Lopez and Manny Lovato of the Los Alamos National Laboratory, Professor Don Koss of the Pennsylvania State University, and Messrs. John McKirgan and Ernie Czyryca of Carderock Division, NSWC.

Approved by:

J. B. Almquist

Brian Almquist
Director, Warhead Dynamics Division

Released by:

Wm Hinckley

William M. Hinckley
Head, Underwater Warheads Technology and Development Department

This page intentionally left blank.

CONTENTS

<i>Heading</i>	<i>Page</i>
Foreword.....	iii
Introduction.....	1
Experimental.....	5
Results.....	8
Discussion.....	19
Conclusions.....	27
References.....	28
Appendix A. MTS Equations and Parameters for HY-100 Steel	A-1
Appendix B. Texture Evolution Compensation.....	B-1

Tables

I. Quadratic Yield Surface Coefficients for a Randomly Textured Isotropic Material and the Current HY-100 Plate.....	8
II. Parameters Used to Calculate g_{0i} and $\hat{\sigma}_i$	15
III. Parameters Used to calculate g_{0eS} and $\hat{\sigma}_{eS0}$	16

Figures

1. Uniaxial Compression and Thin-Walled Torsion Specimens.....	5
2. S_{33} and S_{11} Orientations in Rolled Plate with Schematic of X-Ray Texture Specimen.....	7
3. Pole Figures of HY-100 Steel Plate Measured by X-ray	8
4. Pi-Plane Representation of the Yield Surface for As-Received HY-100 Steel Plate Material	9
5. Quasi-Static Strain Rate Stress-Strain Responses of HY-100 Steel Between 77 and 298 K.....	10
6. Dynamic (high) Strain Rate Stress-Strain Response of HY-100 Steel at 298 K	10
7. Dynamic (high) Strain Rate Stress-Strain Response of HY-100 Steel Between 473 and 873 K.....	11
8. Large Strain Stress-Strain Response of HY-100 Steel Tested in Torsion at 298 K and $\dot{\gamma} \approx 0.01 \text{ s}^{-1}$	12
9. Modified Arrhenius (Fisher) Plot for “Intrinsic” Strengthening Component of the MTS Strength Model For HY-100 Steel.....	14
10. Modified Arrhenius Plot Illustrating the Temperature and Strain-Rate Sensitivity of Structure Evolution Stress, σ_{eS}	16
11. Tangent Modulus Response, $\theta-\sigma$ Plot, Determined from Large Strain Torsion Response	17
12. Comparison Between MTS Prediction and Uniaxial Compression Data for HY-100 Steel.....	19
13. Large Strain Compression Data and MTS Prediction Comparison	21
14. Comparison Between Large Strain Compression and Torsion Data	23
15. Taylor Factor Evolution under Uniaxial Compression and Torsional Loading Paths	25
16. Texture Evolution Manifested by Inverse Pole Figures as a Function of Deformation and Loading Path....	25
17. Stress-Strain Curves Normalized for Loading Path-Dependent Taylor Factor Evolution.....	26
18. Compensating for Texture Evolution in the MTS Strength Model to Rationalize the Dissimilar Stress-Strain Responses Obtained in Compression and Torsion	26

This page intentionally left blank.

INTRODUCTION

The U.S. Navy has initiated a significant effort to develop robust modeling tools to predict structural response of high-strength, high-toughness ship and submarine hull steels to underwater explosive (UNDEX) loading.¹ Naval structures subject to UNDEX loading experience a spectrum of “high-rate” loading conditions, encompassing dynamic buckling at small strains to large strain deformation prior to hull rupture. Both loading conditions realize strain rates prior to “localization” and failure, which are on the order of 100 s^{-1} . The fidelity of structural response prediction relies heavily on the accuracy of the constitutive model and supporting calibration data sets. In particular, constitutive strength models must accurately describe yielding and small strain behavior, in which a rapidly evolving tangent modulus highly influences the onset of dynamic buckling, to large strain bulging and plastic deformation where stress states exist between uniaxial and moderate stress triaxialities. In the latter case, failure may initiate at large plastic strain levels, such as those characterized by $\epsilon_{pl} \rightarrow 1.0$, at which the strain-hardening behavior must be accurately represented. As such, the U.S. Navy is currently interested in investigating and quantifying the constitutive stress-strain response of ship and submarine hull steels (HY-80, HY-100 and HSLA-100) and their associated weld systems.

The constitutive stress-strain response of a U.S. Navy HY-100 steel is characterized employing a three-term mechanical threshold stress (MTS) strength model approach. MTS is a semi-empirical description of the plastic deformation (stress-strain) behavior of (primarily) metals and metallic alloys, and is developed on the basis of two principal concepts. Flow stress, σ , is a metric of the “microstructural” state of a material, i.e., stress is a state variable. A mechanical threshold stress, $\hat{\sigma}$, is also defined as the flow stress at a temperature of absolute zero (i.e., 0 K) such that deformation can be quantified in the absence of thermally activated processes. To accommodate the effects of thermal work, the mechanical threshold stress is scaled based on an Arrhenius description of thermally activated deformation. For brevity, only the salient features of the MTS approach will be discussed. The interested reader, however, is directed to the background and discussions of the approach by Kocks et al.²⁻⁵

The mechanical threshold stress, $\hat{\sigma}$, is commonly expressed as a superposition of flow stress contributions, each component of which characterizes a relevant deformation mechanism:

$$\frac{\hat{\sigma}}{\mu} = \frac{\hat{\sigma}_a}{\mu} + \sum \frac{\hat{\sigma}_j}{\mu} \quad (1)$$

where μ is the temperature-dependent shear modulus and $\hat{\sigma}$ represents the mechanical threshold stress for athermal, or temperature-independent, processes (subscript a) and for the j th individual thermally activated deformation process (subscript j). Phenomenologically, athermal deformation processes primarily consider the “Hall-Petch”-like grain boundary strengthening contribution, whereas the individual thermally activated processes encompass, for example, dislocation interactions with solute (interstitial and solid solution) atoms and second-phase precipitates and dislocation interactions with other dislocations. Recall the mechanical threshold stresses, $\hat{\sigma}_a$ and $\hat{\sigma}_j$, are the flow stress components from athermal and thermally activated processes in the absence of thermal work. The strength model incorporating the MTS concept and rate/thermal effects is outlined below.

Temperature (thermal) effects are incorporated into the MTS strength model framework by a temperature (and strain-rate) dependent scaling factor, S , where:

$$\frac{\sigma_j}{\mu} = S_j(\dot{\epsilon}, T) \cdot \frac{\hat{\sigma}_j}{\mu_0} \quad (2)$$

where μ and μ_0 are temperature-dependent and 0-K shear moduli, respectively, and S is the ratio of temperature-dependent “flow” stress to the mechanical threshold stress $(\sigma_j/\hat{\sigma}_j)$. The scaling factor, S , is derived from an Arrhenius expression relating strain rate to activation energy and temperature:

$$\dot{\epsilon} = \dot{\epsilon}_{0,j} \exp\left(-\frac{\Delta G_j}{kT}\right) \quad (3)$$

assuming a stress-dependent activation (free) energy, ΔG :

$$\Delta G_j = \Delta G \left(\frac{\sigma_j}{\hat{\sigma}_j} \right) = g_{0,j} \mu b^3 \left[1 - \left(\frac{\sigma_j}{\hat{\sigma}_j} \right)^{p_j} \right]^{q_j} \quad (4)$$

where g_0 is a normalized activation energy, b is the burgers vector, p and q are empirical constants related to an “obstacle profile,” $\dot{\epsilon}$ is strain-rate, $\dot{\epsilon}_0$ is a reference strain-rate, k is the Boltzmann constant, and T is absolute temperature. Equations (3) and (4) can be manipulated and re-expressed such that:

$$S_j = \left[1 - \left(\frac{kT}{g_{0,j} \mu b^3} \ln \frac{\dot{\epsilon}_{0,j}}{\dot{\epsilon}} \right)^{\frac{1}{q_j}} \right]^{\frac{1}{p_j}} \quad (5)$$

where S is bounded and obeys $0 \leq S \leq 1$.

The role of temperature (thermal energy) on flow stress is effectively illustrated by equations (2) and (5). Increasing temperature reduces the necessary mechanical energy (stress) for plastic deformation. In addition, the equations comprising (5) illustrate that the temperature dependence of flow stress also gives rise to explicit (strain) rate sensitivity, viz., equation (3). In other words, flow stress, σ , is not a unique quantity with respect to either strain-rate, $\dot{\epsilon}$, or temperature, T . Therefore, numerous combinations of strain rate and temperature, of which many are experimentally tractable, result in an identical value of flow stress. A practical application of this observation is the potential to simulate high strain rates/ambient temperature tests via low strain rates/low temperature tests.

Plastic strain is not explicitly defined within the MTS strength model framework, as per equation (1). Plastic strain is characterized, implicitly, in terms of thermally activated dislocation-dislocation interactions and, specifically, through the mechanical threshold stress, $\hat{\sigma}_\epsilon$. This approach to interpreting plastic strain arises from a viewpoint that the evolution of the dislocation density between, for example, two, constant structure regimes—characterized by $\sigma_{\epsilon,1}$ and $\sigma_{\epsilon,2}$ —is described by plastic strain. This description allows changes in loading path to be accurately represented, e.g., strain rate jumps in which the flow stress changes from $\sigma(\dot{\epsilon}_1)$ to $\sigma(\dot{\epsilon}_2)$ where

$\dot{\epsilon}_1 \neq \dot{\epsilon}_2$. A phenomenological background and method to determine plastic strain over an increment of $\hat{\sigma}_\epsilon$ is described below.

The relationship between plastic strain and structure evolution (dislocation density) is probably best represented, in general, by considering dislocations-dislocation interactions involving the entanglement of dislocations (storage/accumulation) and their mutual annihilation (cross-slip/dynamic recovery). Macroscopically, these interactions are manifested by the macroscopic strain-hardening rate, θ :

$$\theta = \frac{d\hat{\sigma}_\epsilon}{d\epsilon} = \theta_h - \theta_r \quad (6)$$

where θ_h and θ_r are correlated to contributions to strain-hardening from dislocation accumulation and dynamic recovery respectively. Note that dynamic recovery and dislocation accumulation are competitive processes leading to "strain-softening" and "strain-hardening" respectively.

Physically based descriptions for θ_h and θ_r exist; however, the strain-hardening rate is frequently described empirically by:

$$\theta = \frac{d\hat{\sigma}_\epsilon}{d\epsilon} = \theta_0 [1 - f(\hat{\sigma}_\epsilon)] \quad (7)$$

where θ_0 refers to the stage II strain-hardening rate and $f(\hat{\sigma}_\epsilon)$ characterizes an empirically derived dynamic recovery rate. Stage II hardening is typically presumed as fairly insensitive to temperature and rate. At small deformation levels, the strain-hardening rate is approximately the stage II hardening rate, i.e., $\theta \approx \theta_0$, and the dislocation structure is characterized by a small value of $\hat{\sigma}_\epsilon$. With increasing deformation the contribution of $\hat{\sigma}_\epsilon$ may be substantial such that $f(\hat{\sigma}_\epsilon) \rightarrow 1$. In the limit of $f(\hat{\sigma}_\epsilon) \equiv 1$, the strain-hardening rate is zero and a condition of constant flow stress is achieved, i.e., flow stress saturation. In short, the saturation stress response can be interpreted as a balance being achieved between the rates of accumulation and recovery; the net dislocation population (dislocation density) neither increases nor decreases with additional deformation.

Equation (7) can be rewritten and integrated over an appropriate $\hat{\sigma}_\epsilon$ interval to calculate plastic strain. The specific form of ϵ is dependent on the expression describing the strain-hardening rate. The strain-hardening response of HY-100 (and other alloys) is given by a modified *Voce* empirical hardening rule—the *tanh* rule. The *tanh* rule captures the flow stress saturation behavior observed in OFE Cu, and has been similarly employed to represent the strain-hardening behavior of HY-100 (HY-80) steel. The *tanh* rule is given below:

$$\theta = \frac{d\hat{\sigma}_\epsilon}{d\epsilon} = \theta_0 \left(1 - \frac{\tanh \left[\alpha \frac{\hat{\sigma}_\epsilon}{\hat{\sigma}_{\epsilon S}(\dot{\epsilon}, T)} \right]}{\tanh(\alpha)} \right) \quad (8)$$

where σ is an empirical "best-fit" constant which dictates the rate at which saturation is achieved, $\hat{\sigma}_{\epsilon S}$ is a temperature- and rate-sensitive saturation stress, $\hat{\sigma}_\epsilon$ represents a flow stress contribution from dislocation accumulation/annihilation, and θ_0 is an experimentally determined stage II strain-hardening rate. The saturation stress, $\hat{\sigma}_{\epsilon S}$, is derived from the saturation threshold stress, $\hat{\sigma}_{\epsilon S0}$, by :

$$\ln\left(\frac{\dot{\epsilon}_{\epsilon S 0}}{\dot{\epsilon}}\right) = -\frac{\mu b^3 g_{0\epsilon S}}{kT} \ln\left(\frac{\hat{\sigma}_{\epsilon S}}{\hat{\sigma}_{\epsilon S 0}}\right) \quad (9)$$

where $g_{0\epsilon S}$ is a normalized activation energy for dislocation-dislocation interactions. Plastic strain can be determined in closed-form from equation (8):

$$\epsilon = \frac{\tanh(\alpha)}{\theta_0(\tanh^2(\alpha) - 1)} \left(\hat{\sigma}_\epsilon \tanh(\alpha) + \frac{\hat{\sigma}_{\epsilon S}}{\alpha} \ln \left[\tanh(\alpha) \cosh\left(\frac{\alpha \hat{\sigma}_\epsilon}{\hat{\sigma}_{\epsilon S}}\right) - \sinh\left(\frac{\alpha \hat{\sigma}_\epsilon}{\hat{\sigma}_{\epsilon S}}\right) \right] \right) \Big|_{\hat{\sigma}_1}^{\hat{\sigma}_2} \quad (10)$$

A three-term MTS strength model is currently utilized to describe the constitutive stress-strain response of HY-100 steel :

$$\frac{\sigma}{\mu} = \frac{\sigma_a}{\mu} + S_i \cdot \frac{\hat{\sigma}_i}{\mu_0} + S_\epsilon \cdot \frac{\hat{\sigma}_\epsilon}{\mu_0} \quad (11)$$

where the athermal component $\sigma_a \equiv \hat{\sigma}_a$, and subscripts i and ϵ refer to an “intrinsic” barrier to thermally activated dislocation motion and dislocation-dislocation interactions and microstructural evolution with increasing deformation, respectively. Athermal contributions to flow stress can be associated with dislocation interactions with martensite/bainite lath/plate boundaries, i.e., Hall-Petch-type behavior. The intrinsic barrier description encompasses numerous thermally activated deformation processes. Such processes are of principal interest in steels and may potentially include such mechanisms as overcoming the Peierls barrier, dislocation interactions with vacancies, dislocation interactions with solute (interstitial and solid solution) atoms, viz., carbon, oxygen, and nitrogen, and potentially dislocation-carbide (dislocation-particle interactions). Dislocation interactions with other dislocations are also thermally activated. However, unlike the static (constant structure) description of microstructure given by the intrinsic barrier, e.g., “yield” behavior, the $\hat{\sigma}_\epsilon$ term describes the dynamic evolution of the microstructure with increasing deformation, i.e., strain-hardening behavior.

EXPERIMENTAL

The HY-100 steel investigated was received in the form of 25-mm-thick plate. HY-100 is a quenched and tempered NiCrMo steel. The nominal plate composition is 0.16C-2.62Ni-1.32Cr-0.25Mo-0.26Mn-0.14Cu-0.22Si-0.008P-0.009S. The plate was austenitized at 1,195 K for 60 minutes followed by a water quench. Subsequently the plate was tempered at 910 K for 90 minutes followed by water quenching. The HY-100 steel plate was received and tested in this heat-treated condition.

The MTS strength model parameters were determined based on uniaxial compression test results from HY-100 steel. Solid cylindrical test specimens were machined from as-received plate in the short-transverse orientation (Figure 1). Samples were 6.35 mm in diameter and had a 1:1 height-to-diameter aspect ratio. Prior to testing, specimen loading faces were lubricated with molybdenum disulfide. Testing was performed over test conditions encompassing temperatures and strain rates between 77 and 298 K and 0.001 and ~ 2000 s^{-1} respectively. Multiple reloads were performed under room-temperature, quasi-static loading conditions to achieve plastic strains in excess of 1.0. Upon unloading, typically in $\Delta\epsilon = 0.25$ increments, the sample was relubricated to minimize frictional effects; a minimal degree of barreling was observed. At $\epsilon = 0.50$ and 1.0 the deformed specimen was remachined to maintain a 1:1 aspect ratio.

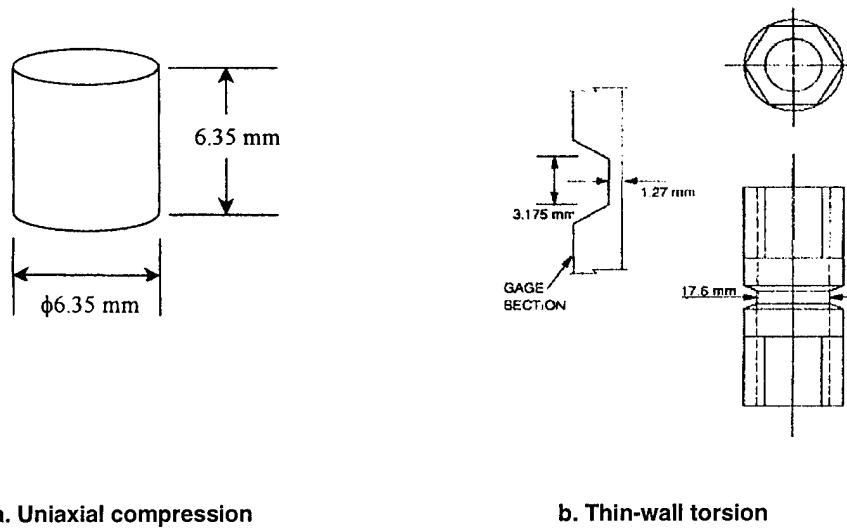


Figure 1. Uniaxial Compression and Thin-Walled Torsion Specimens

“Elevated temperature” testing was also performed at dynamic strain-rates at temperatures of 473, 673, and 873 K. Compression specimens were heated in approximately 5 to 10 minutes under a nominal vacuum of 10^{-3} torr to the test temperature and thereafter “soaked” at the test temperature for an additional 5 minutes prior to testing. However, it should be noted that σ - ϵ data acquired at these elevated temperatures should be considered with caution as the additional tempering during heating and soaking may result in a minor degree of softening of the *original* HY-100 steel martensitic/bainitic microstructure.

Torsion tests of thin-walled tubes at 298 K and 10^{-2} s $^{-1}$ probe the large-strain, shear-stress, shear-strain response. Specimens were machined from as-received plate such that the torsion axis coincided with the transverse plate orientation (Figure 1). Shear stress, τ , and shear strain, γ , for thin-walled tube are given by $\tau = T/2\pi a^2 t$ and $\gamma = a\theta/L$, respectively, where T is torque, a is the mean radius of the tube, t is the wall thickness, θ is the angle of twist, and L is the gage length. A principal motivation for conducting torsion tests is to avoid plastic instability, as occurring in uniaxial tension tests, and frictional effects, as possible in uniaxial compression testing, prior to attaining large plastic strains ($\varepsilon > 1.0$).

In addition, texture of the HY-100 steel plate was probed to infer the extent of anisotropy of the yield surface. Specimens were sectioned parallel to the plate surface (L-LT) in the vicinity of the plate surface and center, and texture was determined in the rolling plane, i.e., perpendicular to the short-transverse orientation (Figure 2). The texture data are discretized by calculating orientation distribution functions (ODF), using the algorithm of Williams, Imhof, Matthies, and Vinel (WIMV analysis).⁶ This ODF information subsequently motivates a yield surface determination via a Taylor and Bishop-Hill analysis.⁷ In short, this procedure calculates a discrete set of stress values comprising the yield surface. These stresses may subsequently be fitted to an existing yield surface formulation. The current study fits the discrete stress values to a quadratic “Hill-48” yield surface formulation,⁸

$$\frac{1}{2} [F(\sigma_{22} - \sigma_{33})^2 + G(\sigma_{33} - \sigma_{11})^2 + H(\sigma_{11} - \sigma_{22})^2 + 2L\sigma_{23}^2 + 2M\sigma_{13}^2 + 2N\sigma_{12}^2] - \sigma^2 = 0 \quad (12)$$

using the method outlined by Maudlin et al.⁷ Expressed in terms of deviatoric stress, equation (12) can be re-expressed as:

$$\frac{1}{2} [(G + H)S_{11}^2 + (F + H)S_{22}^2 + (F + G)S_{33}^2 - 2HS_{11}S_{22} - 2GS_{11}S_{33} - 2FS_{22}S_{33} + 2LS_{23}^2 + 2MS_{13}^2 + 2NS_{12}^2] - \sigma^2 = 0 \quad (13)$$

and the Hill coefficients can be expressed in terms of the deviatoric stresses as:

$$\begin{aligned} S_{11} &\propto \sqrt{\frac{1}{G + H}}, & S_{12} &\propto \sqrt{\frac{1}{2N}}, \\ S_{22} &\propto \sqrt{\frac{1}{H + F}}, & S_{13} &\propto \sqrt{\frac{1}{2M}}, \\ S_{33} &\propto \sqrt{\frac{1}{F + G}}, & S_{23} &\propto \sqrt{\frac{1}{2L}} \end{aligned} \quad (14)$$

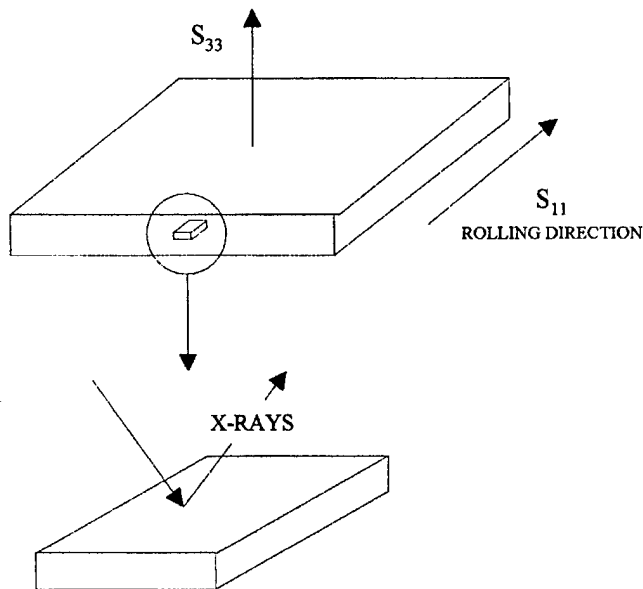


Figure 2. S_{33} and S_{11} Orientations in Rolled Plate with Schematic of X-Ray Texture Specimen

RESULTS

Yield Surface Determination

The yield behavior of the HY-100 steel plate is inferred as isotropic. The coefficients for the quadratic "Hill-48" yield function, deduced from x-ray crystallography measurements of the plate material and the Taylor-Bishop-Hill analysis, are in good agreement with those for a randomly textured, isotropic material deforming by pencil glide (Table I). Pole figures and an inverse pole figure measured at the plate center, shown in Figure 3, indicate m.r.d. (multiple of random distribution) values near 1.0, i.e., a near-random texture. Taylor-Bishop-Hill analysis results are equivalently represented through a π -plane representation, shown in Figure 4. The yield surface represented in Figure 4 is symmetric about $\frac{\sqrt{3}}{2}(S_{22} - S_{11}) = 0$. The shear sub-space corresponding to the HY-100 plate material is spherical, with $\sqrt{3}S_{23} = \sqrt{3}S_{12} = \sqrt{3}S_{13}$, because L , M , and N are essentially identical.

Table I. Quadratic Yield Surface Coefficients for a Randomly Textured Isotropic Material and the Current HY-100 Plate

Texture	F	G	H	L	M	N	Taylor factor
Random (pencil glide)	1.00	1.00	1.10	3.24	3.20	3.21	2.73
Plate (measured)	1.00	0.998	1.13	3.30	3.25	3.31	2.73

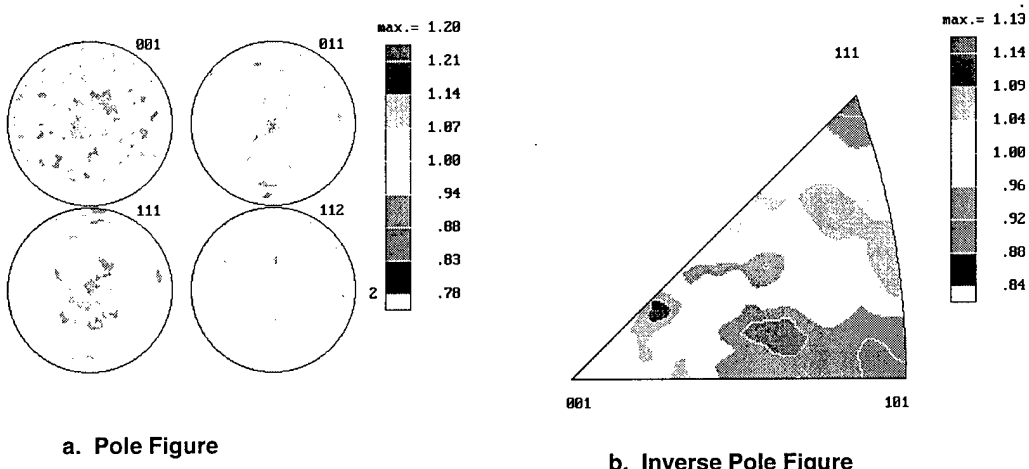


Figure 3. Pole Figures of HY-100 Steel Plate Measured by X-Ray

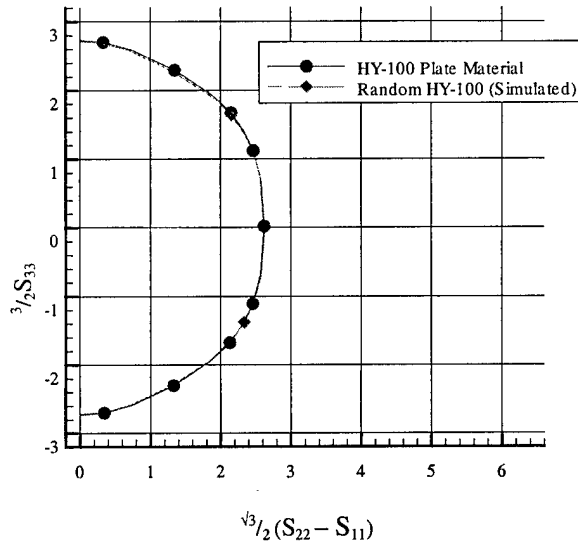


Figure 4. Pi-Plane Representation of the Yield Surface for As-Received HY-100 Steel Plate Material

[Calculated plate material surface is based on x-ray texture measurements.
Randomly textured HY-100 plate is simulated using the Taylor-Bishop-Hill analysis approach.]

Compression Test Results

The MTS strength model, equation (11), is applied to quantify the experimentally determined mechanical response of HY-100 steel shown in Figures 5 through 7. Quasi-static (10^{-3} and 10^{-1} s^{-1}) compressive stress-strain responses at 77, 188, and 298 K are shown in Figure 5. A room-temperature, dynamic strain-rate ($\dot{\epsilon} > 10^3$ s^{-1}) test result is given in Figure 6. Strength model parameters are determined from the data based on a procedure described by Chen and Gray.⁹ Albeit the MTS strength model is a physically based constitutive model describing deformation via the kinetics of dislocation motion, the necessary “material” parameters are often empirically derived.

The mechanical data presented in Figure 5 are characteristic of the deformation behavior of body centered cubic (bcc) metals and alloys. An appreciable increase in the 0.002 offset yield strength is typically observed in bcc metals and alloys with decreasing temperature. Specifically, a rapid increase in the quasi-static yield strength of HY-100 steel from ~ 800 to $\sim 1,300$ MPa, roughly a 40% increase, is recorded between 298 and 77 K respectively. This behavior is commonly attributed to the resistance to dislocation motion afforded by the Peierls barrier and interstitial solute atoms. The effectiveness of these obstacles is very temperature (thermal energy) sensitive. The marked drop in yield strength between 77 and 188 K illustrates that obstacles are increasingly ineffectual in impeding dislocation motion with increasing temperature.

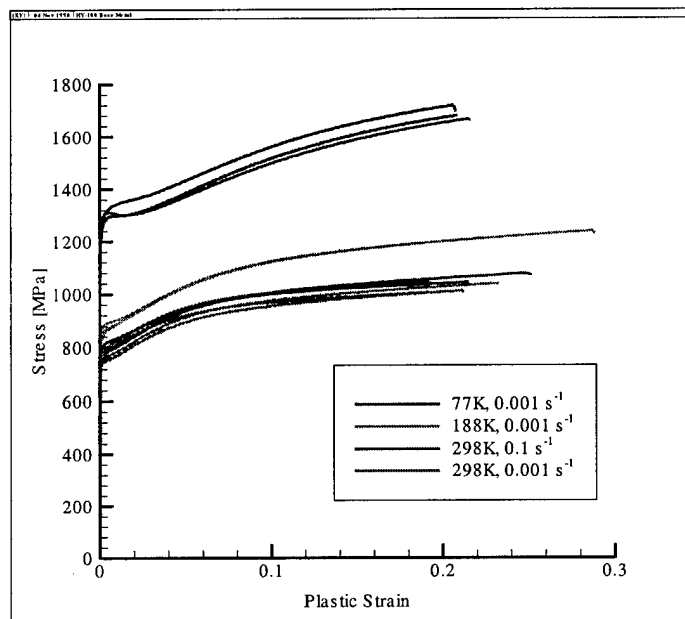


Figure 5. Quasi-Static Strain Rate Stress-Strain Responses of HY-100 Steel between 77 and 298 K

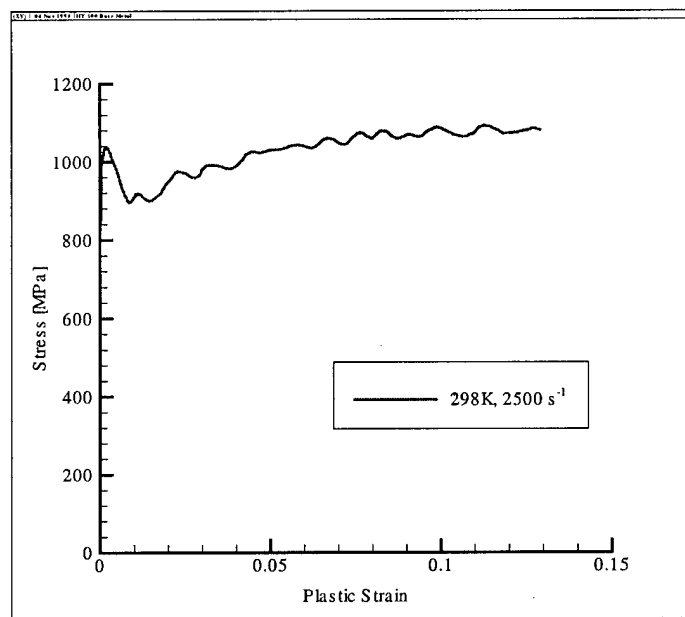


Figure 6. Dynamic (high) Strain Rate Stress-Strain Response of HY-100 Steel at 298 K

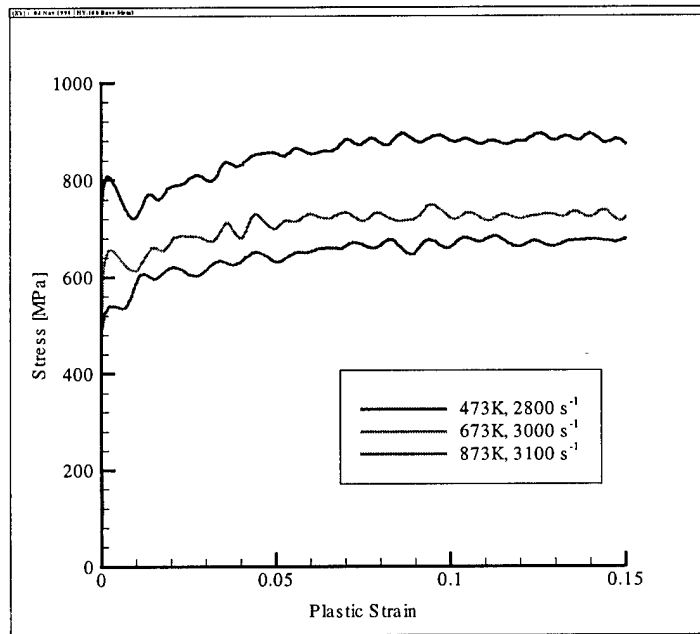


Figure 7. Dynamic (high) Strain Rate Stress-Strain Response of HY-100 Steel between 473 and 873 K

The quasi-static strain-hardening rate, also manifested in Figure 5, increases by a factor of three between 298 and 77 K. Specifically, the hardening rate, ($\theta = d\sigma/d\epsilon$), increases from $\theta_{298K} \sim 600$ MPa/strain to $\theta_{77K} \sim 2,200$ MPa/strain, at a plastic strain of 0.10. These differences in strain-hardening response, although not completely understood, are typically rationalized on the basis of a competition between dislocation accumulation (hardening) and dislocation annihilation (softening). Dislocation accumulation is principally motivated by strain (or deformation) considerations. The latter (softening) process, being sensitive to temperature, for example, through dynamic recovery or cross slip, is less effective at lower temperatures at which thermal energy and the driving force for diffusion are reduced. Although this argument provides rationale for larger strain-hardening rates at lower temperatures, i.e., 77 versus 298 K, the lack of an adequate metallurgical-motivated mathematical description of strain hardening precludes an accurate quantification of this process. As such, the MTS strength model (as well as many other models) relies on a phenomenological description, viz., a Voce-like formulation,¹⁰ of strain hardening.

Dynamic material response, as illustrated in Figure 6, is evaluated similarly to that of the quasi-static behavior. Due to the lack of stress equilibrium at small strains during a split Hopkinson pressure bar test, flow stresses are typically evaluated at plastic strains in excess of 0.01. The room temperature flow stress at $\epsilon_{pl} \sim 0.04$, corresponding to $\sim 2,500$ s⁻¹ strain rate, is approximately 950 MPa. Evaluating this flow stress with respect to the corresponding quasi-static, room temperature flow stress at $\epsilon_{pl} \sim 0.04$ (i.e., $\sigma_{0.04} \sim 860$ MPa) results in an estimated strain rate sensitivity, $m \equiv \Delta(\ln \sigma)/\Delta(\ln \dot{\epsilon}) \sim 0.007$, a typical “ m -value” of high strength steels. At larger strain levels of $\epsilon_{pl} \sim 0.10$ and 0.15 the m -values are essentially identical, viz., $m \sim 0.007$, to that at $\epsilon_{pl} \sim 0.04$. A strain-hardening rate is roughly estimated as $\theta \sim 840$ MPa/strain at a plastic strain of 0.10.

The elevated temperature σ - ϵ response of HY-100 steel was also evaluated under dynamic strain rate conditions, as illustrated in Figure 7. Reiterating, the mechanical response at these elevated temperatures is probably not strictly that of HY-100 steel as a result of the limited tempering and microstructural (phase) evolution sustained during heat-up and soaking. Flow stress at a $\epsilon_{pl} \sim 0.04$ decreases with increasing temperature from ~ 880 MPa at 473 K and $2,500$ s $^{-1}$ to ~ 580 MPa at 873 K and 3100 s $^{-1}$. The hardening rate at $\epsilon_{pl} \sim 0.10$ exhibits an even more precipitous drop between 473 and 873 K from $\theta \sim 788$ MPa/strain at the former temperature, to $\theta \sim 225$ MPa/strain in the latter.

Torsion Test Results

Room-temperature, quasi-static ($\dot{\gamma} \sim 10^2$ s $^{-1}$) torsional stress-strain response of HY-100 steel, illustrated in Figure 8, exhibits good reproducibility. Torsion test data are related to uniaxial compression data by representing both data sets in terms of effective stresses and strains, employing the second invariant of the stress and strain tensor. These second invariants can be expressed as:

$$\bar{\sigma} = \frac{1}{\sqrt{2}} [(\sigma_1 - \sigma_2)^2 + (\sigma_2 - \sigma_3)^2 + (\sigma_3 - \sigma_1)^2]^{1/2}$$

and

$$\bar{\epsilon} = \frac{\sqrt{2}}{3} [(\epsilon_1 - \epsilon_2)^2 + (\epsilon_2 - \epsilon_3)^2 + (\epsilon_3 - \epsilon_1)^2]^{1/2} \quad (15)$$

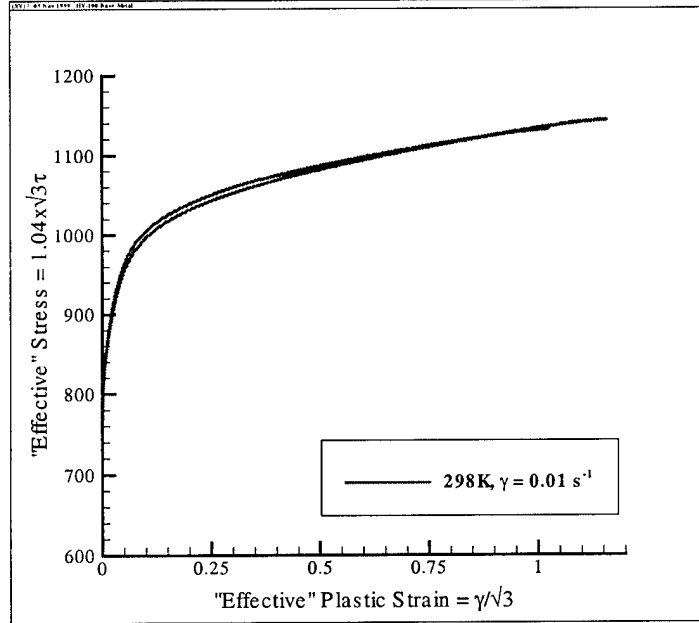


Figure 8. Large Strain Stress-Strain Response of HY-100 Steel Tested in Torsion at 298 K and $\dot{\gamma} \approx 0.01$ s $^{-1}$

The relationships between effective stress and strain and uniaxial compression (or tension) and torsion are listed below:

Effective Quantities	Uniaxial	Torsion
$\bar{\sigma}$	σ	$\sqrt{3}\tau$
$\bar{\epsilon}$	E	$\gamma/\sqrt{3}$

Effective stress and strain values are subsequently “adjusted” to account for texture by comparing yield strength ratios in compression and shear, $\sigma_{33}:\sigma_{13}$, between an isotropic von Mises material and the current HY-100 plate. Yield strength ratios are calculated using Hill coefficients, cf., equation (14). A von Mises material is characterized by $F = G = H = 1$ and $L = M = N = 3$. For example, the yield strength ratio between compression and shear, $\sigma_{33}:\sigma_{13}$, can be written as:

$$\frac{\sigma_{33}}{\sigma_{13}} = \sqrt{\frac{2M}{F+G}} \quad (16)$$

For a von Mises material, this ratio is $\sqrt{3} = 1.732$. The ratio exhibited by the current plate material is 1.804. On this basis the plate material is expected to yield at a stress level approximately 4% higher than that presumed assuming a von Mises yield criterion. Therefore, the 0.002 offset yield strength is predicted as:

$$\bar{\sigma} = 1.04 \times \sqrt{3} \times \tau \quad (17)$$

For the current plate material this value is $\bar{\sigma} \approx 800$ MPa.

MTS Parameters

The MTS strength model parameters are determined, based on a procedure described by Chen and Gray⁹, using mechanical data from Figures 5 through 7. Evaluation of the dynamic material response, i.e., Figures 6 and 7, also involved considering adiabatic heating effects. Although the MTS strength model is a physically based constitutive model describing deformation via the kinetics of dislocation motion, the necessary “material” parameters are empirically derived. An approach to determine MTS strength model parameters is given below, with the corresponding equations and parameters for HY-100 steel summarized in Appendix A.

The temperature-dependent shear modulus for HY-100 steel is given by Chen and Gray¹¹ as an empirical relation in the form:

$$\mu = \mu_0 - \frac{D}{\exp\left(\frac{T_0}{T}\right) - 1} \quad (18)$$

where μ_0 , D , and T_0 are in essence empirical parameters. The values of μ_0 , D , and T_0 are 71,460 MPa, 2,910 MPa, and 204 K respectively.

The athermal stress, σ_a , contribution in equation (11) is estimated as $\sigma_a \sim 40$ MPa; no rigorous analysis was performed to arrive at this value of σ_a . However, assuming Hall-Petch-type boundary strengthening as the principal active athermal strengthening mechanism, an athermal stress on the order of 40 MPa is not unreasonable. For example, Tomita¹² determined for a 0.2C-NiCrMo steel a Hall-Petch constant characterizing the martensite packet size of $k_y = 0.578 \text{ MN}\cdot\text{m}^{-3/2}$. Assuming packet sizes on the order of 100 μm , the Hall-Petch effect is $k_y d^{1/2} \sim 50$ MPa.

Thermally activated deformation of HY-100 steel is generically characterized within the context of the "intrinsic" term, $\hat{\sigma}_i$, and is assumed to be primarily the Peierls barrier, carbon interstitial solute atom strengthening, and dislocation strengthening in the quenched and tempered martensite. A normalized activation energy of $g_{0i} \sim 1.161$ and a mechanical threshold stress of $\hat{\sigma}_i \sim 1341$ MPa are determinable based on a "Fisher" diagram¹³ (Figure 9 and Table II). Specifically, g_{0i} and $\hat{\sigma}_i$, are determined when mechanical data are presented in a Fisher plot format:

$$\left(\frac{\sigma - \sigma_a}{\mu} \right)^{p_i} = \left(\frac{\hat{\sigma}_i}{\mu_0} \right)^{p_i} - \left(\frac{\hat{\sigma}_i}{\mu_0} \right)^{p_i} \cdot \left(\frac{1}{g_{0i}} \right)^{1/q_i} \left[\frac{kT}{\mu b^3} \ln \left(\frac{\dot{\epsilon}_{0i}}{\dot{\epsilon}} \right) \right]^{1/q_i} \quad (19)$$

This procedure does, however, involve making an a priori assumption as to values of the glide obstacle profile parameters, p_i and q_i , and the reference strain-rate, $\dot{\epsilon}_{0i}$. Empirical observations and guidance given by reference (2) suggest p_i and q_i be equated to 1/2 and 3/2, respectively, whereas $\dot{\epsilon}_{0i}$ is chosen as 10^{13} s^{-1} . A single set of constant values of p_i , q_i , and $\dot{\epsilon}_{0i}$ for HY-100 presumes all active deformation mechanisms can be effectively represented by a single thermally activated deformation mechanism over a range of strain rates and temperatures.

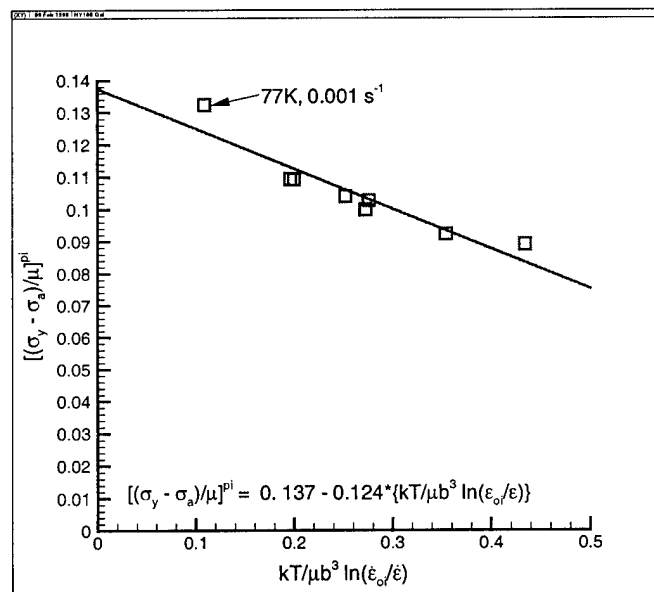


Figure 9. Modified Arrhenius (Fisher) Plot for "Intrinsic" Strengthening Component of the MTS Strength Model for HY-100 Steel

[Mechanical threshold stress, $\hat{\sigma}_i$, and normalized activation energy value, g_{0i} , are determinable from this plot.]

Table II. Parameters Used to Calculate g_{0i} and $\hat{\sigma}_i$.

$kT/\mu b^3 \ln(\dot{\epsilon}_{0i}/\dot{\epsilon})$	$[(\sigma_y - \sigma_a)/\mu]^{pi}$	T (K)	$\dot{\epsilon}$ (s ⁻¹)	σ_y (MPa)	μ (MPa)
0.10907963	0.132357801	77	0.001	1,288	71,239
0.200156472	0.109237414	188	0.001	875	69,975
0.252494489	0.104077917	298	0.1	782	68,499
0.276002618	0.102736741	298	0.001	763	68,499
0.196370459	0.109411649	298	2500	860	68,499
0.272794009	0.099951907	473	2800	700	66,063
0.3545421	0.0924051	673	3000	580	63,240
0.434362062	0.089142151	873	3100	520	60,404

The structure evolution parameters, comprising equations (2), (5), (8) and (9), also describe thermally activated deformation, and as such are similarly determined by analyzing the so-called “Fisher”-plot behavior. Inherent complexity and a lack of a specific understanding in the evolution of the dislocation population in highly dislocated martensitic/bainitic steels also necessitates relying on previous experience in “simpler” material systems.^{2,14} Therefore, the structure evolution glide obstacle profile parameters, p_ϵ and q_ϵ , and the reference strain rates, $\dot{\epsilon}_{0c}$ and $\dot{\epsilon}_{0\epsilon S}$, were initially chosen based on those for bcc tantalum and tantalum-tungsten alloys¹⁴ and assigned values of 2/3, 1, 10⁷ s⁻¹, and 10⁷ s⁻¹ respectively. The normalized activation energy (saturation), $g_{0\epsilon S}$, and the mechanical threshold stress associated with “saturation” of the evolving structure, i.e., dislocation population, $\hat{\sigma}_{\epsilon S0}$, are calculated using a Fisher-type plot approach. Equation (9) is re-expressed in the form:

$$\ln \hat{\sigma}_{\epsilon S} = \ln \hat{\sigma}_{\epsilon S0} - \frac{kT}{\mu b^3} \frac{1}{g_{0\epsilon S}} \ln \frac{\dot{\epsilon}_{\epsilon S0}}{\dot{\epsilon}} \quad (20)$$

Figure 10 is a graphical representation of equation (20) with the parameters given in Table III.

The threshold saturation stress at a given temperature and strain-rate, $\hat{\sigma}_{\epsilon S}$, can be estimated by extrapolating the tangent modulus response curve, i.e., $\theta - \sigma_\epsilon$ response, to a zero strain-hardening rate, i.e., $\theta \equiv 0$; for example, see Figure 11. The contributions of athermal hardening and intrinsic strengthening, both of which are independent of structure evolution (strain), are subtracted from the overall flow stress to arrive at a value of σ_ϵ :

$$\hat{\sigma}_\epsilon = \left(\frac{\sigma}{\mu} - \frac{\sigma_a}{\mu} - \frac{S_i}{\mu_0} \hat{\sigma}_i \right) \frac{\mu_0}{S_\epsilon} \quad (21)$$

where σ is given by the experimentally determined stress-strain data. Based on Figure 10, $\hat{\sigma}_{\epsilon S0}$ and $g_{0\epsilon S}$ are estimated as 790 MPa and 0.112 respectively.

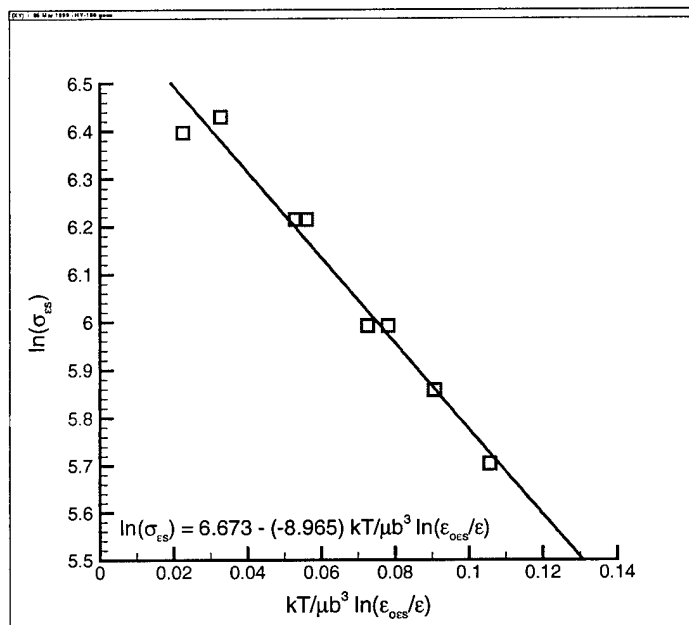


Figure 10. Modified Arrhenius Plot Illustrating the Temperature and Strain-Rate Sensitivity of Structure Evolution Stress, $\sigma_{\varepsilon s}$
 [Threshold stress, $\hat{\sigma}_{\varepsilon s0}$, and the normalized activation energy value, $g_{0\varepsilon s}$, are determinable from this plot.]

Table III. Parameters Used to Calculate $g_{0\varepsilon s}$ and $\hat{\sigma}_{\varepsilon s0}$

$\ln(\hat{\sigma}_{\varepsilon s})$	$kT/\mu b^3 \ln(\varepsilon_{\varepsilon s0}/\dot{\varepsilon})$	$\hat{\sigma}_{\varepsilon s}$ [MPa]	$\dot{\varepsilon}$ [s^{-1}]	T [K]	μ [MPa]
6.3969	0.02252	600	0.001	77	71,239
6.2146	0.05597	500	0.001	188	69,975
6.4297	0.03016	620	2,500	298	68,499
5.9915	0.07250	400	0.1	298	68,499
5.8579	0.09063	350	0.001	298	68,499
6.2146	0.05372	500	2,800	473	66,063
5.9915	0.07985	400	3,000	673	63,240
5.7038	0.10844	300	3,100	873	60,404

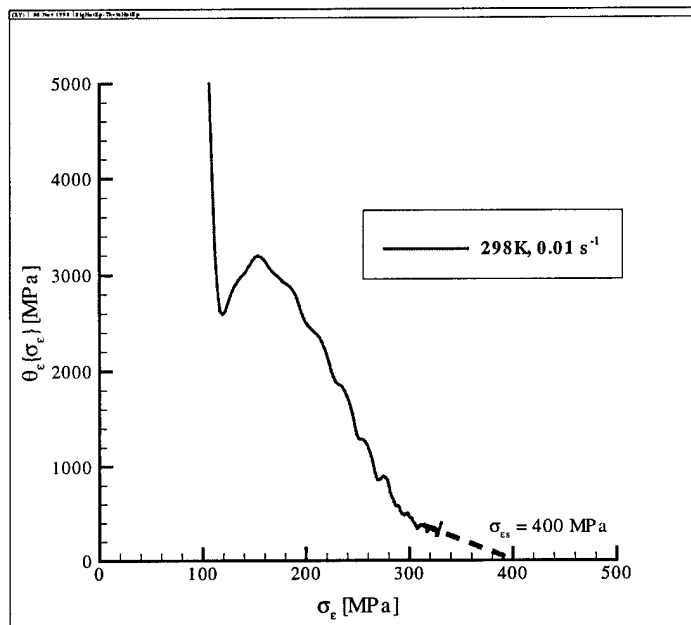


Figure 11. Tangent Modulus Response, θ - σ Plot, Determined from Large Strain Torsion Response

[Superimposed is an extrapolation to a zero strain-hardening level (flow stress saturation), characterized by $\sigma_{\epsilon s}$.]

The saturation-rate parameter, α , in the Voce-like \tanh strain-hardening rule was determined as $\alpha \equiv 2$ based on previous experience with other alloys systems and then subsequently optimized through an iterative process. Similarly, the stage II strain hardening rate, θ_0 , is given as by an empirical relationship:

$$\theta_0 = 5102.4 - 2.0758 T \quad (22)$$

where T is temperature in kelvins and θ_0 is in units of MPa/strain. Unlike the basis in thermally activated deformation of the mechanical threshold stress, α and the \tanh hardening rule are completely empirical in nature. Admittedly, these descriptions of the structure evolution are the weakest aspects of the strength model.

Adiabatic heating effects, relevant under dynamic (high strain-rate) loading conditions, are represented within the MTS strength model framework via the deformation temperature in strengthening contributions affected by thermal activation. For HY-100 steel, adiabatic heating is presumed to occur if the strain rate is in excess of $\dot{\epsilon} \sim 500 \text{ s}^{-1}$. Temperature increases due to adiabatic heating are expressed by:

$$\Delta T = \frac{\Psi}{\rho C_P} \int \sigma(\epsilon) \cdot d\epsilon \quad (23)$$

where Ψ can be analogized with the fraction of work converted into heat, as opposed to producing strain hardening. For HY-100 steel, Ψ is assumed equal to 0.95. The density of HY-100 steel is being assumed equivalent to iron, such that $\rho = 7.86 \text{ Mg/m}^3$, and the temperature-dependent specific heat is being given by the empirical relationship:¹¹

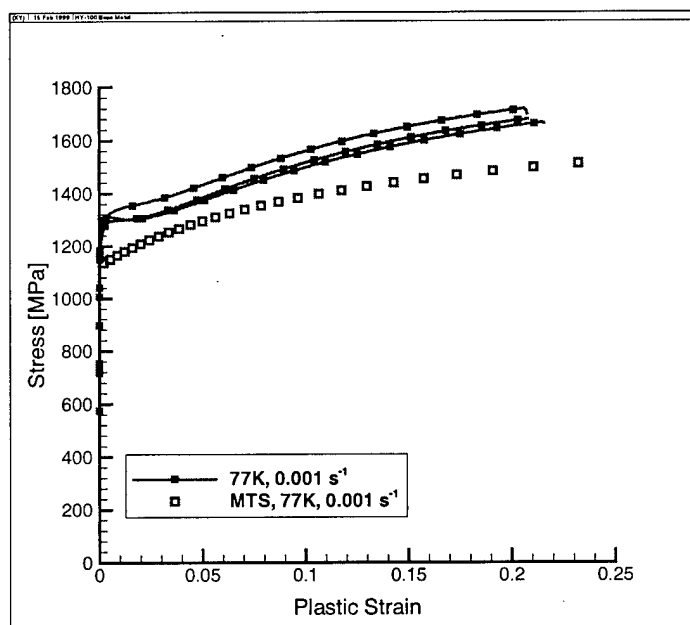
$$C_P = 0.09278 + 7.454 \times 10^{-4} \cdot T + \frac{12404}{T^2} \quad (24)$$

in units of $\text{MPa m}^3/\text{Mg/K}$.

DISCUSSION

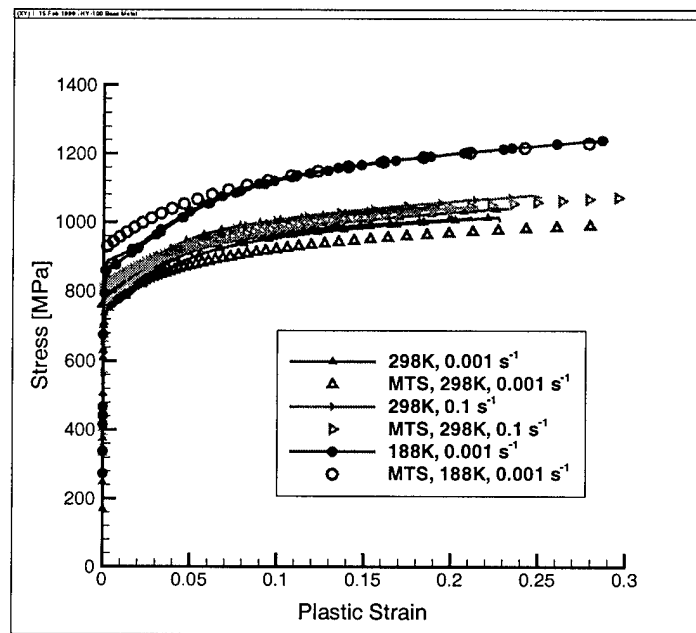
Constitutive Behavior of HY-100 Steel

The MTS framework, in general, well characterizes the deformation response of HY-100 steel near the onset of yielding (Figure 12). Both temperature and strain rate sensitivities of the yield strength are captured, and their inter-relationship is described by an Arrhenius expression, Equation (3). A single Arrhenius expression is employed to characterize thermally activated deformation over the investigated temperature/strain-rate regime, cf., $\hat{\sigma}_i$ and Equation (19). No dominant thermally activated process, however, is identified as affecting dislocation motion. Rather an “effective” obstacle is prescribed, encompassing the Peierls effect at low (cryogenic) temperatures and solute strengthening at ambient (298 K) and elevated temperatures, through the parameters, g_{0i} , p_i , q_i , $\dot{\epsilon}_{0i}$, and $\hat{\sigma}_i$.

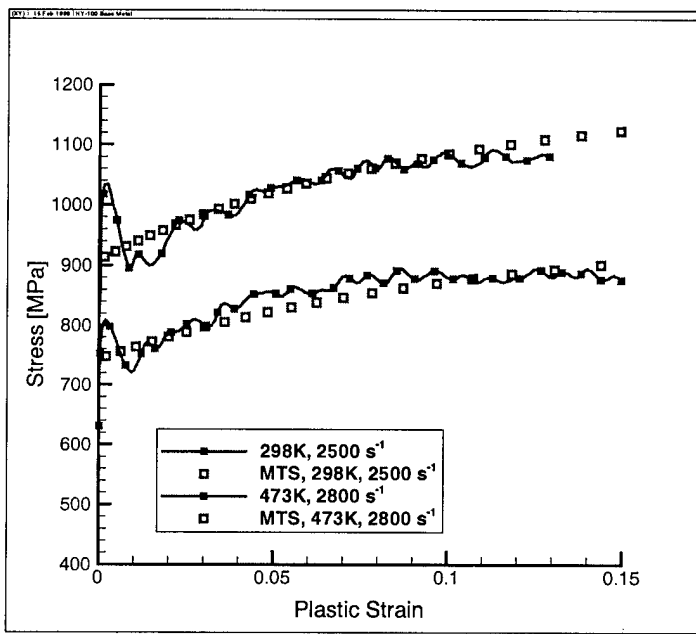


a. At 77K

Figure 12. Comparison between MTS Prediction and Uniaxial Compression Data for HY-100 Steel (Quasi-Static Response) (Page 1 of 2)



b. At 188 and 298 K



c. At 298 and 473 K

Figure 12. Comparison between MTS Prediction and Uniaxial Compression Data for HY-100 Steel (Quasi-Static Response) (Page 2 of 2)

A marked deviation between experiment and MTS prediction is, however, observed for HY-100 steel for a test condition at 77 K and 10^{-3} s $^{-1}$ (Figure 12). The relative difference between yield strength determined by experiment and MTS prediction is $\approx 24\%$. MTS calculation underpredicts yield strength. Although the nature of this disparity is not currently understood, potential explanations may include (a) the presence of a distinct deformation mechanism that is not sufficiently represented by the current single “effective” obstacle description and (b) the role of slip mode, i.e., pencil glide versus restricted glide, on yield strength.¹⁵ Both rationale require modifying the current three-term MTS strength model approach, either through incorporating a temperature/rate-sensitive strength term, as for tantalum¹⁴ and zirconium¹⁶, or amending a Taylor-like factor. The latter has been considered employing polycrystalline plasticity calculations.^{15,17,18} In short, these calculations suggest low-temperature deformation, if dominated by restricted glide, i.e., {110}<111> slip, can result in $\approx 15\%$ larger yield strengths than those predicted if assuming low-temperature deformation occurring via <111>-pencil glide slip. Although not accounting for the disparity between experiment and prediction in full, considering the geometric nature of slip improves agreement between experiment and is incorporated into the thermally activated deformation framework.

Strain-hardening behavior is less well characterized than is yield strength by the MTS strength model. In particular, the compressive stress-strain response illustrated in Figure 13 exhibits increasing deviation between model prediction and experiment at increasingly larger deformation levels, i.e., at large plastic strains under room-temperature deformation conditions. The nature of this discrepancy arises from an a priori assumption (and enforcement) of flow stress saturation. HY-100 steel, however, exhibits strain-hardening behavior that decreases from the initial stage II value, θ_0 , to an apparent relatively constant, finite strain-hardening rate. This constant strain-hardening rate is often referred to as linear or “stage IV” strain hardening. Similar linear hardening behavior has been observed in other steels¹⁹ and aluminum alloys²⁰ and is of potential importance in loading scenarios involving large strain deformation.

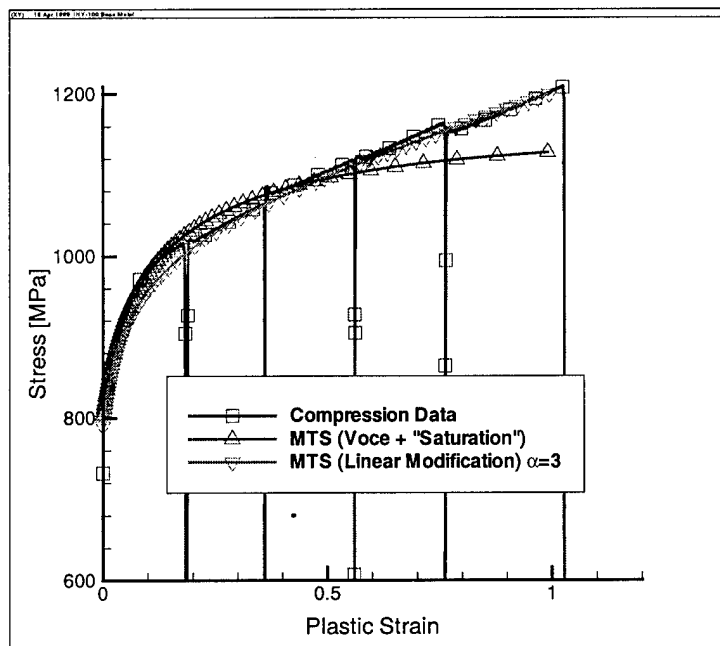


Figure 13. Large Strain Compression Data and MTS Prediction Comparison
 [Employing (a) modified Voce hardening rule imposing flow stress saturation and
 (b) modified Voce hardening rule with linear strain-hardening component]

Large strain uniaxial compression response of HY-100 steel tends to indicate a linear hardening rate of ~ 200 to 300 MPa/strain is achieved at flow stresses greater than 960 MPa. This finite degree of strain hardening, or lack of flow stress saturation, at large deformation levels gives rise to the lack of agreement between model and experiment, and also indicates the current Voce-like *tanh* hardening rule may not adequately capture structure evolution. In lieu of a complex dislocation-based description of strain hardening encompassing, for example, cross-slip and dislocation accumulation and annihilation within low energy dislocation cell structures,²¹⁻²³ an empirical description of hardening analogous to that of the Voce rule is proposed.

An alternative strain-hardening formulation based on the Voce-like expression currently utilized within the MTS strength model framework is formulated to describe the linear strain-hardening behavior of HY-100 steel. Linear hardening is captured by a Voce-like expression by assuming the initiation of stage IV hardening marks the termination of stage III in the absence of flow stress saturation. In other words, rather than stage II transitioning via stage III to flow stress saturation, as currently described in the MTS strength model, stage II transitions via stage III to linear, stage IV hardening. A modification to an existing *tanh* strain hardening rule (equation (8)) is proposed to provide (a) a general method to represent either flow stress saturation or stage IV (linear hardening) behavior, (b) an improved stress-strain prediction at both small and large strain, and (c) a formulation that can be readily integrated to yield a closed-form, analytic solution of $\varepsilon = f(\sigma)$. The linear hardening rule is imposed such that achieved is a continuous increase in flow stress with increasing strain and a constant hardening rate at large strains (and flow stresses) (Figure 13).

A proposed “1st order” modification to the *tanh* strain-hardening rate expression (with linear stage IV strain-hardening) is given below as:

$$\theta = \frac{d\hat{\sigma}_e}{d\varepsilon} = \theta_0 \left\{ 1 - \tanh \left(\alpha \frac{\hat{\sigma}_e}{\hat{\sigma}_{eS}} \right) \right\} + \theta_{IV} \tanh \left(\alpha \frac{\hat{\sigma}_e}{\hat{\sigma}_{eS}} \right) \quad (25)$$

Analogous to equation (8), the modified strain-hardening rate term (equation (25)) is composed of hyperbolic tangent terms. This modified hardening expression takes advantage of the former *tanh* rule’s good description of stress-strain response at small strains levels. Furthermore stage IV hardening at large strain levels can be better represented by the linear hardening rate modification.

The contribution due to linear (stage IV) hardening is present as the second term on the right hand side of equation (25). Saturation stress, as present in the Voce-like (e.g., *tanh*) expressions, is effectively redefined as the stress level at which flow stress saturation would occur in the absence of linear hardening. In the absence of stage IV hardening, the saturation stress, as originally intended, in the Voce-like (e.g., *tanh*) expression can be introduced into equation (25) and the value for the stage IV strain-hardening rate, θ_{IV} , set equal to zero. Conceptually, the above expression can be envisaged as stage III behavior, as represented by the first *tanh*(...) term, provides a transition between a first regime of linear strain-hardening, i.e., stage II (θ_0), to a second regime of much smaller strain-hardening, i.e., stage IV (θ_{IV}).

Identical to equation (8) equation (25) can be integrated directly with respect to $\hat{\sigma}_e$ to yield to a closed-form analytic solution for strain:

$$\varepsilon = \frac{\theta_0 \hat{\sigma}_e}{\theta_0^2 - (\theta_0 - \theta_{IV})^2} - \frac{-(\theta_0 - \theta_{IV})}{\alpha/\hat{\sigma}_{eS} (\theta_0^2 - (\theta_0 - \theta_{IV})^2)} \ln \left[-(\theta_0 - \theta_{IV}) \sinh \left(\alpha \frac{\hat{\sigma}_e}{\hat{\sigma}_{eS}} \right) + \theta_0 \cosh \left(\alpha \frac{\hat{\sigma}_e}{\hat{\sigma}_{eS}} \right) \right] \quad (26)$$

which can be assessed over a finite stress interval between $\sigma_{\varepsilon,1}$ and $\sigma_{\varepsilon,2}$. Recall again that within the MTS framework stress is the internal state variable and, as such, $\varepsilon = f(\sigma)$. As mentioned previously $\hat{\sigma}_{\varepsilon S}$ is redefined to characterize the threshold stress at which stage III hardening transitions to stage IV, in the absence of flow stress saturation. Parameters for this modified hardening rule (equation 26) are shown below:

σ	2.5
θ_0	7,600 MPa/strain
$\hat{\sigma}_{\varepsilon S0}$	822 MPa
θ_{IV}	200 MPa/strain

Torsion Versus Uniaxial Compression and Texture Evolution

Uniaxial compression and torsion tests provide constitutive data from relatively well-defined stress-states, e.g., uniaxial or pure shear, respectively, and are both utilized when available. Figure 14 illustrates that the mechanical responses derived from uniaxial compression and torsion are in good agreement up to an effective plastic strain of ~ 0.40 . However, increasing deviation in effective stress values are observed with increasing plastic strain. The compressive stress-strain response appears to exhibit near-linear hardening at large strain levels, whereas the torsion-derived stress-strain behavior appears to approach flow stress saturation.

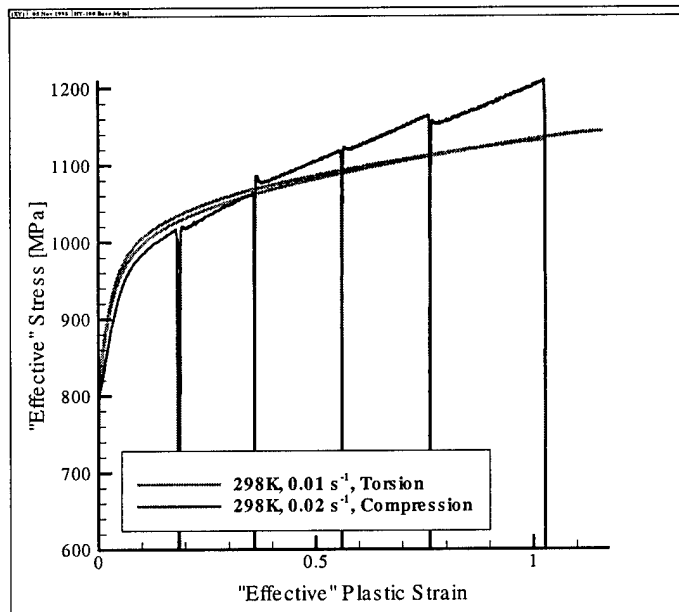


Figure 14. Comparison between Large Strain Compression and Torsion Data
[Increasing deviation between response is observed with increasing deformation.]

Polycrystalline plasticity calculations, using the LApp code,⁶ suggest deformation-induced texture evolution results in a “harder” material when the deformation path is uniaxial compression, as opposed to torsion.^{18,24} Figures 15 and 16 illustrate the Taylor and texture factor evolutions as a function of deformation for a uniaxial

compression and torsion. The increase in the Taylor factor from ~ 2.73 to ~ 2.85 ($\varepsilon \sim 1.0$) in compression indicates textural hardening occurs. In pure shear a decreasing Taylor factor from ~ 2.73 to ~ 2.66 ($\varepsilon \sim 1.0$) is observed and tends to indicate textural softening occurs. Furthermore, the calculation results illustrate that differences in Taylor factor between compression and shear are exacerbated with increasing deformation; e.g., $M_{\text{compression}}/M_{\text{torsion}}$ increases with increasing deformation. These contrasting Taylor factor evolutions in part rationalize the differences in stress-strain response observed between uniaxial compression and torsion with increasing deformation.

Stress-strain curves (Figure 17) illustrate that compensating for deformation-induced texture evolution brings into better agreement the uniaxial compression and torsion mechanical responses; the procedure used to account for texture evolution is presented in Appendix B. Qualitatively, the similar strain-hardening rates exhibited in compression and torsion suggest the hardening mechanisms are similar between loading paths and can be modeled with an identical hardening rule and parameters by the MTS strength model.

The linear strain-hardening modified MTS strength model prediction of the room temperature, quasi-static compression data is re-evaluated to include texture evolution effects. Taylor factor evolution is incorporated into the structure evolution term, such that:

$$\hat{\sigma}_\varepsilon = \hat{\sigma}_\varepsilon' / M^* \quad (27)$$

where M^* is the normalized Taylor factor, as given in Appendix B. MTS parameters correspond to those presented above. These MTS strength model parameters, as well as those listed in Appendix A, can be considered as texture compensated and may be applied in representing effective stress-strain response in conjunction with appropriate texture, i.e., Taylor factor, evolution rules, e.g., equations (B2) and (B3), for the current HY-100 steel plate material. Figure 18 illustrates MTS strength model predictions with and without texture evolution and the effect of texture evolution (softening) under a torsional loading path. This figure also shows that incorporating texture evolution into the constitutive model may explain in part the apparently dissimilar stress-strain curves measured in uniaxial compression (from which the MTS parameters are determined) and torsion. However, the fair agreement between torsion and the MTS prediction illustrates accurate descriptions of texture evolution in torsion and compression are still required as well as a more robust implementation of texture evolution in the strength model.

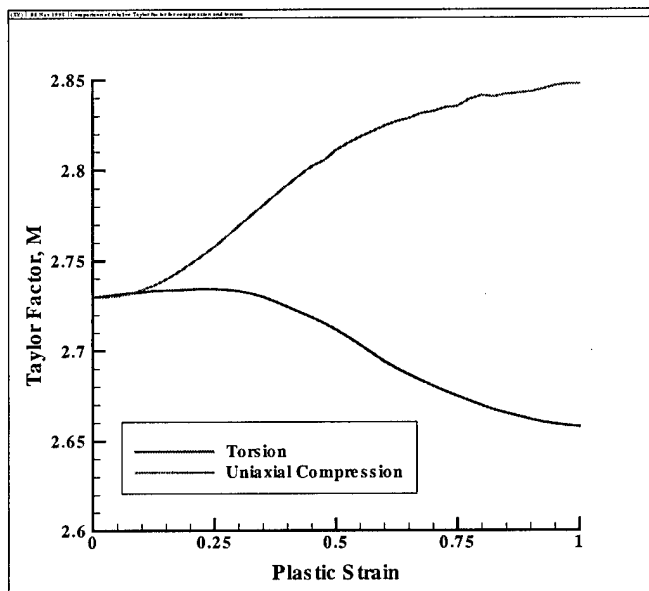
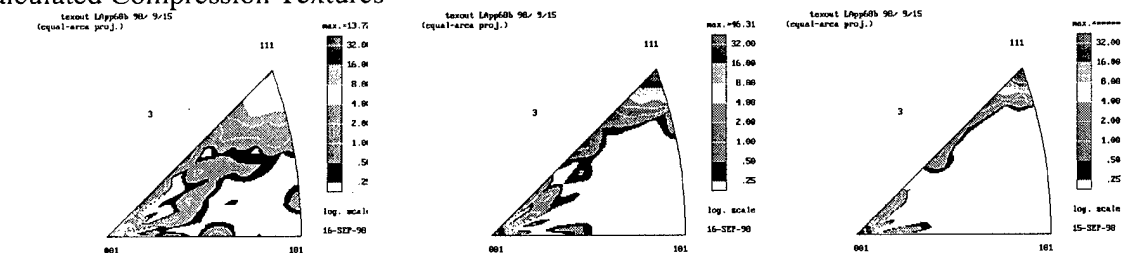


Figure 15. Taylor Factor Evolution under Uniaxial Compression and Torsional Loading Paths

Calculated Compression Textures



Calculated Torsion Textures

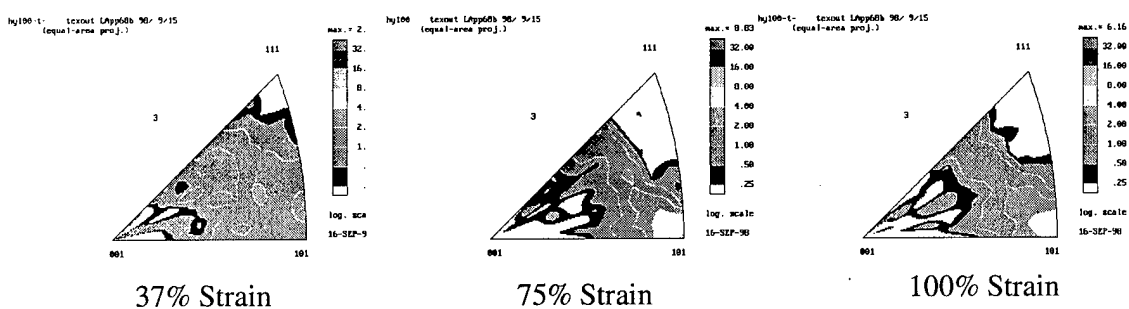


Figure 16. Texture Evolution Manifested by Inverse Pole Figures as a Function of Deformation and Loading Path

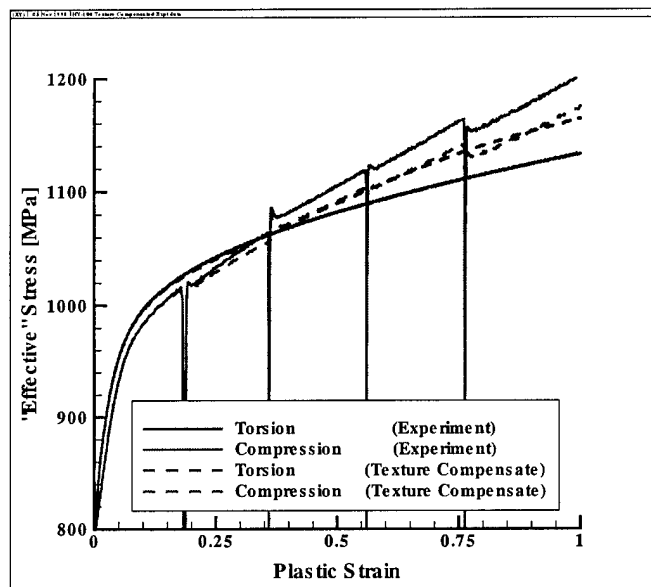


Figure 17. Stress-Strain Curves Normalized for Loading-Path-Dependent Taylor Factor Evolution

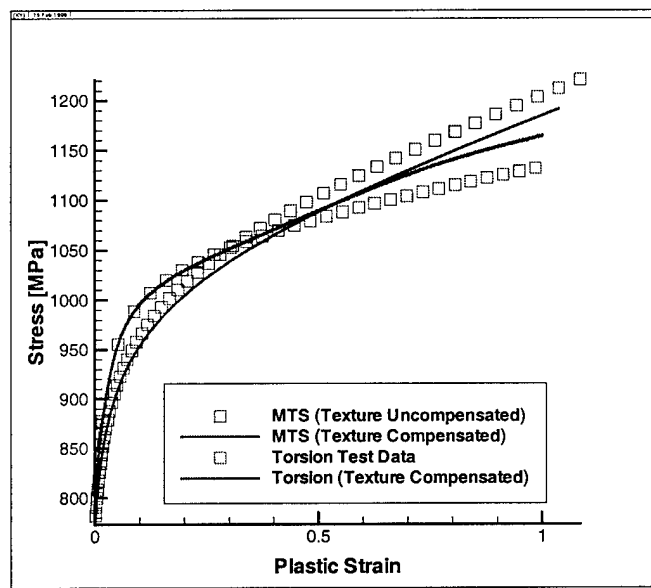


Figure 18. Compensating for Texture Evolution in the MTS Strength Model to Rationalize the Dissimilar Stress-Strain Responses Obtained in Compression and Torsion

CONCLUSIONS

The MTS strength model framework is well-suited to characterizing the constitutive mechanical response of metals and alloys. A three-term MTS strength model currently characterizes Navy HY-100 steel. Featured within the three-term MTS model are constant structure considerations, such as athermal and thermally activated deformation mechanisms, and structure evolution (strain-hardening) considerations.

Athermal strengthening is presumed associated with martensite/bainite lath boundary or Hall-Petch-type behavior. Thermally activated processes encompass the intrinsic Peierls barrier and solute strengthening due principally to interstitial atoms, such as carbon, nitrogen, and oxygen. Additionally, "constant structure" and thermally activated deformation includes the initial dislocation population within the tempered martensite laths. Structure evolution involves the dynamic processes of dislocation accumulation and annihilation. Analogous to the concept of thermally activated deformation of the "constant structure," temperature/rate effects are modeled for structure evolution via an Arrhenius expression. However, structure evolution, *viz.*, the competition between dislocation accumulation and annihilation, is modeled solely from an empirical basis and utilizes a Voce-like expression. The Voce-like strain-hardening (structure-evolution) expression appears to be deficient in accurately modeling material mechanical response at large deformation levels and as such is a principal limitation of the MTS strength model.

A principal motivation to modify the existing *tanh* (Voce-like) hardening rule, as currently implemented in the MTS strength model, is to improve the predicted constitutive stress-strain behavior at both small and large strain levels, with primary emphasis on improving the large strain stress-strain prediction. The existing *tanh* hardening rule well approximates a material's small strain ($\bar{\epsilon} < 0.10$) stress-strain response. However, the fidelity of this *tanh* rule is degraded at larger strain levels ($\bar{\epsilon} > 0.20 \sim 0.30$). A modification to this hardening rule is proposed to improve the large strain prediction while retaining the good small-strain prediction characteristics of the original *tanh* model.

Agreement among effective stress-strain data obtained from different loading paths is improved when experimental stress-strain data is compensated for deformation-induced texture. The current MTS framework, equations (1) through (11), does not include texture considerations in the structure evolution rule, *i.e.*, the *tanh* model. As such, the MTS strength model incorporates both dislocation hardening/softening and texture evolution into the structure evolution rule. Polycrystalline plasticity calculations illustrate that deformation-induced texture evolution, manifested by a strain-dependent Taylor factor, becomes marked at deformation levels of $\bar{\epsilon} > 0.20$. Furthermore, notable deviation between effective stress-strain responses is observed between uniaxial compression and torsion in the absence of compensating deformation for texture evolution. Subsequent to considering texture evolution in the stress-strain response, very good agreement is achieved between uniaxial compression and torsion.

An implication of the current observations and results is that improved agreement between effective stress-strain response over arbitrary loading paths can be achieved if texture evolution is compensated for within the experimental data and strength model. The example presented above illustrated the agreement between effective stress-strain behavior for a near-random HY-100 steel deforming over a well-defined loading path involving either uniaxial compression or torsion when texture evolution was coupled to structure evolution. Highly textured materials, such as tantalum, may exhibit significant deformation-induced texture evolution and may require that for accurate stress-strain representation the constitutive strength model include a structure evolution term to account for Taylor factor evolution.

REFERENCES

1. H.U. Mair and R.K. Garrett, Jr., in *Constitutive Laws: Theory, Experiments and Numerical Implementation*, eds. A.M. Rajendran and R.C. Batra, CIMNE, Barcelona, Spain (1995) 1-17.
2. U.F. Kocks, A.S. Argon, and M.F. Ashby, *Thermodynamics and Kinetics of Slip, Progress in Materials Science*, Vol. 19, Pergamon Press, NY, (1975), p. 291.
3. U.F. Kocks, *J. Engng. Mater. Tech.*, 98 (1976) 76-85.
4. H. Mecking and U.F. Kocks, *Acta Metall.*, 29 (1981) 1865-1875.
5. P.S. Follansbee and U.F. Kocks, *Acta Metall.*, 36 (1988) 81-93.
6. U.F. Kocks, J.S. Kallend, A.D. Rollett, and S.I. Wright, LA-CC-89-18, (1994) p. 92.
7. P.J. Maudlin and S.K. Schiferl, LA-12611-MS, UC-000, (1993) p. 48.
8. R. Hill, *The Mathematical Theory of Plasticity*, Oxford University Press, London, 1950.
9. S.R. Chen and G.T. Gray III, LA-UR-96-3534 (1996) p. 44.
10. E. Voce, *J. Inst. Metals*, 74 (1948) 537-562.
11. S.R. Chen and G.T. Gray III, Personal communication, 1998.
12. Y. Tomita, *Mater. Sci. Tech.*, 7 (1991) 299-306.
13. C.W. MacGregor and J.C. Fisher, *J. Appl. Mech.*, 68 (1946) A11-A16.
14. S.R. Chen and G.T. Gray III, *Metall. Mater. Trans.*, 27A (1996) 2994-3006.
15. A. Beaudoin, Jr., personal communication, 1998.
16. S.R. Chen and G.T. Gray III, *J. Phys. IV France*, 7 (1997) C3-741-C3-746.
17. U.F. Kocks, M.G. Stout, and A.D. Rollett, in *Strength of Metal and Alloys*, ICSMA 8, eds. P.O. Kettunen, T.K. Lepisto, and M.E. Lehtonen, Pergamon Press, Oxford, 1988, pp. 25-34.
18. R.K. Garrett, Jr., D.M. Goto, and J. Bingert, Unpublished data, (1998).
19. X.F. Fang and W. Dahl, *Mater. Sci. Engng.*, A203 (1995) 14-25.
20. A.D. Rollett, Ph.D. thesis, Drexel University, Philadelphia, PA 1988.

21. D. Kuhlmann-Wilsdorf, *Metall. Trans. A*, 16A (1985) 2091-2108.
22. D. Kuhlmann-Wilsdorf and N. Hansen, *Metall. Trans. A*, 20A (1989) 2393-2397.
23. X.F. Fang and W. Dahl, *Mater. Sci. Engng.*, A203 (1995) 36-45.
24. U.F. Kocks, M.G. Stout, and A.D. Rollett, in *Strength of Metal and Alloys*, ICSMA 8, eds. P.O. Kettunen, T.K. Lepisto, and M.E. Lehtonen, Pergamon Press, Oxford, 1988, pp. 25-34.

This page intentionally left blank.

Appendix A

MTS EQUATIONS AND PARAMETERS FOR HY-100 STEEL

This page intentionally left blank.

$$\bullet \frac{\sigma}{\mu} = \frac{\sigma_a}{\mu} + S_i(\dot{\epsilon}, T) \frac{\hat{\sigma}_i}{\mu_0} + S_\epsilon(\dot{\epsilon}, T) \frac{\hat{\sigma}_\epsilon}{\mu_0}$$

Where: $\sigma_a = 40 \text{ MPa}$

$$\frac{\hat{\sigma}_i}{\mu_0} = 0.01877 \text{ (or } \hat{\sigma}_i = 1,341 \text{ MPa)}$$

$$\bullet \mu = \mu_0 - \frac{2910 \text{ MPa}}{\exp\left(\frac{204 \text{ K}}{T}\right) - 1}$$

Where: $\mu_0 = 7.146 \times 10^4 \text{ MPa}$

$$\bullet S_i(\dot{\epsilon}, T) = \left\{ 1 - \left[\frac{kT}{\mu b^3 g_{0i}} \ln\left(\frac{\dot{\epsilon}_{0i}}{\dot{\epsilon}}\right) \right]^{1/q_i} \right\}^{1/p_i}$$

Where: $\frac{k}{b^3} = 0.9047 \text{ MPa / K}$

$$k = 1.38 \times 10^{-23} \text{ J/K}, b = 2.48 \times 10^{-10} \text{ m}$$

$$\dot{\epsilon}_{0i} = 1 \times 10^{13} \text{ s}^{-1}$$

$$g_{0i} = 1.161$$

$$q_i = 3/2, p_i = 1/2$$

$$\bullet S_\epsilon(\dot{\epsilon}, T) = \left\{ 1 - \left[\frac{kT}{\mu b^3 g_{0\epsilon}} \ln\left(\frac{\dot{\epsilon}_{0\epsilon}}{\dot{\epsilon}}\right) \right]^{1/q_\epsilon} \right\}^{1/p_\epsilon}$$

Where: $\dot{\epsilon}_{0\epsilon} = 1 \times 10^7 \text{ s}^{-1}$

$$g_{0\epsilon} = 1.6$$

$$q_\epsilon = 1, p_\epsilon = 2/3$$

$$\bullet \frac{d\hat{\sigma}_\epsilon}{d\epsilon} = \theta_0(\dot{\epsilon}, T) \cdot \left[1 - \frac{\tanh\left(\alpha \frac{\hat{\sigma}_\epsilon}{\hat{\sigma}_{\epsilon s}(\dot{\epsilon}, T)}\right)}{\tanh(\alpha)} \right]$$

Where:

$$\theta_0 = 5102.4 - 2.0758 \cdot T; \text{ MPa}$$

$$\alpha = 2$$

$$\bullet \ln \frac{\dot{\epsilon}}{\dot{\epsilon}_{0\epsilon s}} = \frac{\mu b^3 g_{0\epsilon s}}{kT} \ln \frac{\hat{\sigma}_{\epsilon s}}{\hat{\sigma}_{\epsilon s 0}}$$

Where: $g_{0\epsilon s} = 0.112$

$$\hat{\sigma}_{\epsilon s 0} = 782 \text{ MPa}$$

$$\dot{\epsilon}_{0\epsilon s} = 1 \times 10^7 \text{ s}^{-1}$$

$$\bullet \Delta T = \frac{\Psi}{\rho C_p} \int \sigma(\varepsilon) d\varepsilon; \quad \text{when } \dot{\varepsilon} \geq 500 \text{ s}^{-1}$$

Where: $\Psi = 0.95$

$\rho = 7.86 \text{ Mg/m}^3$

$$C_p = 0.09278 + 7.454 \times 10^{-4} \cdot T + \frac{12404}{T^2};$$

MPa m³/Mg/K

Appendix B

TEXTURE EVOLUTION COMPENSATION

This page intentionally left blank.

Texture evolution in the experimental data is accommodated by normalizing the experimentally determined flow stress by a deformation-dependent relative Taylor factor. The differences in stress-strain response amongst loading paths are addressed by compensating experimental uniaxial compression and torsion data for texture, cf., equation (17), and texture evolution. Experimental data are normalized for texture evolution through:

$$\sigma^{\text{NoTexture}} = \sigma^{\text{Expt}} / M^* \quad (\text{B1})$$

where $\sigma^{\text{NoTexture}}$ corresponds to texture-compensated experimental data, σ^{Expt} refers to the original experimental data, and M^* is the appropriate normalized Taylor factor and equal to $M(\varepsilon)/M_0$. The M -evolution over a uniaxial compression loading path is expressed in terms of a sixth-order polynomial (cf., Figures 15 and 16):

$$M(\varepsilon)_{\text{compression}} = -1.3141\varepsilon^6 + 3.6953\varepsilon^5 - 3.2263\varepsilon^4 + 0.369\varepsilon^3 + 0.6234\varepsilon^2 - 0.0297\varepsilon + 2.7302 \quad (\text{B2})$$

Similarly, the evolution of M over a pure shear loading path is expressed as (cf., Figures 15 and 16):

$$M(\varepsilon)_{\text{torsion}} = -0.1632\varepsilon^6 - 0.5208\varepsilon^5 + 2.1803\varepsilon^4 - 2.0809\varepsilon^3 + 0.5296\varepsilon^2 - 0.0184\varepsilon + 2.7306 \quad (\text{B3})$$

The initial Taylor factor at $\varepsilon = 0$ is $M_0 = 2.73$. The resulting $\sigma^{\text{NoTexture}} - \varepsilon$ curves are illustrated in Figure 16.

This page intentionally left blank.

DISTRIBUTION*Paper copies:*

CHIEF OF NAVAL RESEARCH
 ATTN CODE 332 DR G YODER
 BALLSTON CENTRE TOWER ONE
 800 NORTH QUINCY ST
 ARLINGTON VA 22217-5660

1

CHIEF OF NAVAL RESEARCH
 ATTN CODE 333 DR J GOLDWASSER
 BALLSTON CENTRE TOWER ONE
 800 NORTH QUINCY ST
 ARLINGTON VA 22217-5660

1

COMMANDER CARDEROCK DIVISION
 NAVAL SURFACE WARFARE CENTER
 ATTN CODE 614 MR E CZYRYCA
 9500 MACARTHUR BLVD WEST
 BETHESDA MD 20817-5700

1

COMMANDER CARDEROCK DIVISION
 NAVAL SURFACE WARFARE CENTER
 ATTN CODE 0115 DR W MESSICK
 9500 MACARTHUR BLVD WEST
 BETHESDA MD 20817-5700

1

CD ROM Copies:

DIRECTOR
 NAVAL RESEARCH LABORATORY
 ATTN CODE 6382 DR A GELTMACHER
 4555 OVERLOOK AVE SW
 WASHINGTON DC 20375

1

DIRECTOR
 NAVAL RESEARCH LABORATORY
 ATTN CODE 6382 DR P MATIC
 4555 OVERLOOK AVE SW
 WASHINGTON DC 20375

1

COMMANDING OFFICER
 AFRL / MUNITIONS DIRECTORATE
 ATTN DR J C FOSTER JR
 101 W EGLIN BLVD STE 136
 EGLIN AFB FL 32542-6810

1

COMMANDING OFFICER
 ARMY RESEARCH LABORATORY
 ATTN AMSRL-WM-TD DR A M RAJENDRAN
 MATERIAL MODELING TEAM BLDG 4600
 ABERDEEN PROVING GRD MD 21005-5069

1

COMMANDER CARDEROCK DIVISION
 NAVAL SURFACE WARFARE CENTER
 ATTN CODE 614 MR J MCKIRGAN
 9500 MACARTHUR BLVD WEST
 BETHESDA MD 20817-5700

1

LOS ALAMOS NATIONAL LABORATORY
 ATTN DR G T GRAY III
 MST-8 MAIL STOP G755
 LOS ALAMOS NM 87545

1

LOS ALAMOS NATIONAL LABORATORY
 ATTN DR S R CHEN
 MST-8 MAIL STOP G755
 LOS ALAMOS NM 87545

1

LOS ALAMOS NATIONAL LABORATORY ATTN MR J BINGERT MST-6 MAIL STOP G770 LOS ALAMOS NM 87545	1	ALLEGHENY LUDLUM TECHNICAL CENTER ATTN DR T J SALSGIVER BRACKENRIDGE PA 15014-1597	1
LOS ALAMOS NATIONAL LABORATORY ATTN DR P MAUDLIN T-3 MAIL STOP B216 LOS ALAMOS NM 87545	1	NEWPORT NEWS SHIPBUILDING ATTN MR G STEELE 4101 WASHINGTON AVE NEWPORT NEWS VA 23607-2770	1
SANDIA NATIONAL LABORATORY ATTN DR M HORSETMEYER MAIL STOP 9405 P O BOX 969 LIVERMORE CA 94551	1	NEWPORT NEWS SHIPBUILDING ATTN MR C J JOSEPH AIRPORT PLAZA ONE STE 1100 2711 SOUTH JEFFERSON DAVIS HWY ARLINGTON VA 22202-4028	1
UNIV OF CALIFORNIA LAWRENCE LIVERMORE NATIONAL LABORATORY ATTN DR D LASSILA MAIL CODE L-099 P O BOX 808 LIVERMORE CA 94551-0808	1	<i>e-Mail:</i> Jrike@dtic.mil Lochness@jhunix.hcf.jhu.edu	
PENNSYLVANIA STATE UNIVERSITY ATTN PROFESSOR D KOSS METALS SCIENCE & ENGINEERING DEPT 202A STEIDLE BLDG UNIVERSITY PARK PA 16802	1	Internal: <i>Paper copies:</i>	
CARNEGIE MELLON UNIVERSITY ATTN PROFESSOR T ROLLETT WEAN HALL 3327 5000 FORBES AVE PITTSBURGH PA 15213-2890	1	TD 1 420 1	
UNIV OF PITTSBURGH AT JOHNSTOWN ATTN PROFESSOR J BANDSTRA 225 ENGINEERING & SCIENCE BLDG JOHNSTOWN PA 15904	1	<i>CD ROM copies:</i> 420 3 8230 1 840L 1	
ALLEGHENY LUDLUM TECHNICAL CENTER ATTN DR T J RICKERT BRACKENRIDGE PA 15014-1597	1		